Modeling of nanoscale liquid mixture transport by density functional hydrodynamics

Oleg Yu. Dinariev and Nikolay V. Evseev*
Schlumberger Moscow Research, 13 Pudovkina Street, Moscow, Russia
(Received 9 December 2016; published 13 June 2017)

Modeling of multiphase compositional hydrodynamics at nanoscale is performed by means of density functional hydrodynamics (DFH). DFH is the method based on density functional theory and continuum mechanics. This method has been developed by the authors over 20 years and used for modeling in various multiphase hydrodynamic applications. In this paper, DFH was further extended to encompass phenomena inherent in liquids at nanoscale. The new DFH extension is based on the introduction of external potentials for chemical components. These potentials are localized in the vicinity of solid surfaces and take account of the van der Waals forces. A set of numerical examples, including disjoining pressure, film precursors, anomalous rheology, liquid in contact with heterogeneous surface, capillary condensation, and forward and reverse osmosis, is presented to demonstrate modeling capabilities.

DOI: 10.1103/PhysRevE.95.063307

I. INTRODUCTION

Multiphase compositional hydrodynamic processes in small pores and microchannels are encountered in many areas in industry and science. For instance, they are relevant for various natural processes in biology, geology, hydrology, and technical processes ranging from fuel cells to oil recovery and CO_2 sequestration. To date there is a number of techniques used for multiphase flow modeling, including possible application for multiphase flows in pores. Most commonly known modeling methods are (listed in alphabet order) Cahn-Hilliard equation method, embedded interface, free boundary problem, lattice Boltzmann, level set, phase field, pore network, smooth particle hydrodynamics, and volume of fluid (VOF). Various approaches have individual strong and weak sides as they address different challenges of the general problem. Our overview of the listed methods can be found elsewhere [1,2]. We also refer the reader to the reviews found in Refs. [3–8].

In this work, various multiphase compositional problems are treated in the frame of the density functional hydrodynamics (DFH). The basic concepts of the method were published by Dinariev [9,10]; some of the latest publications are [1,2,11–15]. The historical overview of the DFH can be found in Ref. [2]. Here we present a very general overview of this theory.

The basic idea of the density functional theory (DFT), which is the foundation of DFH, is representation of energy of a heterogeneous system as a functional of densities of chemical components constituting the system. The first consistent results in this direction are related to Thomas-Fermi model of electron gas developed in 1927; see review in the book by Parr and Yang [16]. But the genuine interest in DFT arose in 1964–1965 after the works by Kohn and his coauthors; see, e.g., Ref. [17]. Since then a lot of works on this subject were published. The 1998's Nobel Prize in chemistry was awarded to Walter Kohn, the major contributor in DFT development. Currently, the DFT is successfully applied in quantum chemistry, nuclear physics, physics of semiconductors, superconductivity, and diamagnetics. In his Nobel lecture, Kohn [18] identified 13 various directions of possible DFT generalization, among them heterogeneous systems and Helmholtz free energy at finite temperatures. Initial formulation of DFT was developed for static systems, and Kohn's ideas were successfully implemented to describe equilibrium states of various fluids, including the molecular structure of liquids [19–22]. The obtained results comprise analysis of static one-, two-, and three-phase states, wettability, and contact angles [23–28]. Also, there has been a significant progress in modeling of specific nanopore phenomena like capillary condensation and adsorption at pore walls [29–32].

The applications of DFT to static fluid problems are largely associated with nonlocal formulations of energy functional. However, while the dynamic extension of general nonlocal DFT is straightforward from a theoretical point of view [2,33], it is not computationally effective. In order to obtain a constructive and computationally efficient approach for dynamic problems, it is necessary to make certain changes in DFT formulation. Introduction of the DFT into hydrodynamics of multiphase compositional mixtures, developed by Dinariev [9,10] and eventually called DFH, can be considered as an example of such DFT optimization suitable for numerical simulations. Previously, several authors [34–39] modeled various multiphase hydrodynamic phenomena using order parameter functional methods. The DFH method does not use order parameter concept.

DFH uses classical mass, momentum, and energy conservation laws with specific constitutive relations. These constitutive relations are derived to ensure consistency between hydrodynamic and thermodynamic descriptions of multiphase compositional system in the frame of the density functional approach. The specific expression for the density functional uses square gradients of molar densities, which enables description of surface tension. Thermodynamic state of the mixture is described by means of bulk and surface thermodynamic potentials, where the latter enables correct description of liquid-solid interaction, i.e., wettability and adsorption. DFH is successfully applied to hydrodynamic phenomena in two- and three-phase compositional mixtures with phase transitions (including liquid-liquid, gas-liquid, gas-solid, liquid-solid, etc.), adsorption, surfactants, and non-Newtonian rheology [1,2,15,40].

*nevseev@slb.com

The present work describes extension of the DFH for a set of hydrodynamic phenomena, which take place at nanometer scale. To make such extension possible, it was necessary to take account of different phenomena related to disjoining pressure [41,42]. This was done by introducing in DFH external potential forces in the vicinity of solid surfaces. Further, we developed implementation of modified DFH equations within numerical simulator. Then we demonstrated by numerical modeling that proposed modifications can be used for effective description of several classical nanometer scale effects, such as static and dynamic behavior of liquid films, film precursors, and forward and reverse osmosis.

The detailed discussion of the developed DFH extension is given in Sec. II. A range of numerical simulations of multiphase nanometer scale phenomena is presented in Sec. III. The overall summary and discussion of further possibilities of the DFH is outlined in Sec. IV.

II. THEORETICAL CONCEPTS AND EQUATIONS

Here we propose further extension of the DFH method to incorporate a range of phenomena, which are observed for the liquid mixtures at nanometer scale. The main instrument of this extension is introduction of specific forces acting on chemical components of the mixture in the vicinity of the solid surfaces. These forces are assumed to be characterized by potentials, which are variable in space but do not depend on time. This assumption is sufficient to describe a set of nanoscale physical phenomena without introducing significant changes in the already existing DFH numerical simulator; however, DFH method itself does not put specific restrictions on potentials and can be further extended in future.

Let us begin with description of basic fields, which characterize instantaneous state of mixture. It is important to remember that DFH is based on continuum mechanics, so it does not consider individual molecules, but operates with continuously distributed physical quantities. It is convenient to use, as basic fields, the following quantities: chemical component molar densities n_i, mass velocity v_a, and internal energy density u. Further, we discuss briefly how these parameters are defined. The summation over repeated indices is implied everywhere.

Let us consider a homogeneous mixture of M chemical components inside a spatial region D of volume V_D. The region contains N_{iD} $(i = 1,\dots,M)$ of each type of molecule. To avoid large numbers, the quantities N_{iD} are measured in moles and by definition $n_i = N_{iD}/V_D$. If the mixture is inhomogeneous, one can define n_i locally by establishing a small volume limit, such as $n_i = n_i(t,x^a) = \lim_{V_D\to 0}(N_{iD}/V_D)$. Here, t is time and x^a are Cartesian coordinates. Like elsewhere in continuum mechanics, the small volume limit is understood as the convergent procedure with V_D being small, but still larger than the molecular volume.

By counting the flow rate of molecules through a small area inside the mixture, one can define the component flux $I_{ia} = I_{ia}(t,x^b)$. The component fluxes are used to calculate the mass flux $I_a = m_i I_{ia}$, where m_i is the molar mass of the ith component. By introducing mass density $\rho = m_i n_i$ it is possible to define mass velocity $v_a = \rho^{-1} I_a$. Component flux I_{ia} can be represented as a combination of transport term $n_i v_a$ and diffusion flux Q_{ia}:

$$I_{i\,a} = n_i v_a + Q_{ia}, \tag{1}$$

where by definition, diffusion flux does not influence net mass transfer,

$$m_i Q_{i\,a} = 0. \tag{2}$$

The total energy E_D of the molecules inside region D is a sum of kinetic and potential energy (the latter being the result of molecular interaction and influence of external potential forces). The energy density can be calculated by establishing the small volume limit, $\varepsilon = \varepsilon(t,x^a) = \lim_{V_D\to 0}(E_D/V_D)$. Internal energy density can be defined by subtracting the kinetic energy density and the external potential energy from the total energy:

$$u = u(t,x^a) = \varepsilon - \tfrac{1}{2}\rho v_a v_a - n_i\phi_i, \tag{3}$$

where $\phi_i = \phi_i(x^a)$ are external potentials associated with chemical components in the mixture. The introduction of these potentials constitutes the extension of the previous DFH theory.

For a mixture occupying some spatial region D we assume the existence of the entropy functional,

$$S_D = S_D[u\,,n_i]. \tag{4}$$

Here the entropy $S_D = S_D(t)$ is determined at any moment of time by the internal energy field $u = u(t,x^a)$ and density fields $n_i = n_i(t,x^a)$. The general expression Eq. (4) is substantiated in statistical mechanics [43]. In Eq. (4) and below, the term "functional" is used in the sense that the considered quantity depends on the spatial fields (and not on point values) at a particular moment of time.

The explicit expression for functional Eq. (4) is introduced into continuum mechanics in general (and into hydrodynamics in particular) from other branches of science, such as physical chemistry and statistical physics. In many cases, it is possible to use the following functional, which is considered an appropriate approximation to the exact though implicit definition of the entropy functional in statistical physics (see discussion in Ref. [2], pp. 39–57):

$$S_D = \int_D \theta dV + \int_{\partial D} s_* dA, \tag{5}$$

$$\theta = s(u,n_i) - 2^{-1}\alpha_{ij}(n_k)\partial_a n_i \partial_a n_j, \tag{6}$$

where ∂D is the boundary surface for the region D (when the region is finite), $s = s(u,n_i)$ is the entropy bulk density for homogeneous mixture, α_{ij} is the positive-definite symmetric matrix, and $s_* = s_*(u,n_i)$ is the entropy surface density (not equal to zero if ∂D is a contact surface with some immobile solid).

The model, which is presented in Eqs. (5) and (6), is adequate for many important phenomena, but it is not universal. Up to now, it was successfully used to simulate multiphase multicomponent phenomena with or without phase transitions, surfactants, mixtures with solid phases (e.g., gas hydrates or solid particles), and thermal effects [2]. However, it is not sufficient for the simulation of structured liquids (e.g., liquid crystals), which require more complex expressions for the entropy functional.

Before moving on to dynamic problems it is appropriate to discuss equilibrium states of the mixture. Such states correspond to conditional critical points of the functional Eq. (4) under the constraints that the potential energy U_D and the amount of components N_{iD} are fixed, i.e.:

$$U_D = \int_D (u + n_i\phi_i)dV + \int_{\partial D} u_* dA, \tag{7}$$

$$N_{iD} = \int_D n_i dV, \tag{8}$$

where $u_* = u_*(u,n_i)$ is internal energy surface density. At this point, it is appropriate to recollect some of the classical thermodynamic equations [44]:

$$u = Ts + \kappa_i n_i - p, \tag{9}$$

$$du = Tds + \kappa_i dn_i, \tag{10}$$

$$dp = sdT + n_i d\kappa_i, \tag{11}$$

where T is absolute temperature, κ_i is chemical potential of ith chemical component of the mixture, and p is hydrostatic pressure. Also, note the following useful relations, which result from Eq. (10):

$$\left(\frac{\partial s}{\partial u}\right)_{n_i} = T^{-1}, \left(\frac{\partial s}{\partial n_i}\right)_{u\,,\,n\,j\neq i} = -T^{-1}\kappa_i. \tag{12}$$

We assume that functions $s_* = s_*(u,n_i)$ and $u_* = u_*(u,n_i)$ are related in a way similar to Eq. (12),

$$\left(\frac{\partial s_*}{\partial u_*}\right)_{n_i} = T^{-1}. \tag{13}$$

As follows from the above statements, the equilibrium states of the mixture can be found as solutions of the variational equation having the form

$$\delta S_D - \lambda_0 \delta U_D - \lambda_i \delta N_{iD} = 0, \tag{14}$$

where λ_0,λ_i are Lagrange multipliers. In order to obtain explicit equations for equilibrium states, it is convenient to calculate variational derivatives using Eq. (12):

$$\Theta_0 = \frac{\delta S_D}{\delta u} = T^{-1}, \tag{15}$$

$$\Theta_i = \frac{\delta S_D}{\delta n_i} = -T^{-1}\kappa_i - 2^{-1}\frac{\partial \alpha_{jk}}{\partial n_i}\partial_a n_j \partial_a n_k + \partial_a(\alpha_{ij}\partial_a n_j). \tag{16}$$

Now using Eqs. (5)–(8), (15), and (16) one can derive equilibrium equations

$$\Theta_0 = \lambda_0, \tag{17}$$

$$\Theta_i = \lambda_0\phi_i + \lambda_i, \tag{18}$$

together with the following boundary conditions at ∂D

$$\left(\frac{\partial s_*}{\partial u}\right)_{n_i} = \lambda_0 \left(\frac{\partial u_*}{\partial u}\right)_{n_i}, \tag{19}$$

$$\left(\frac{\partial s_*}{\partial n_i}\right)_{u,n\,j\neq i} + \alpha_{ij} l^a \partial_a n_j = \lambda_0 \left(\frac{\partial u_*}{\partial n_i}\right)_{u,n_{j\neq i}}, \tag{20}$$

where l^a is the internal normal unit vector at the boundary surface ∂D.

Note that in accordance with Eq. (17), the temperature is constant everywhere in equilibrium state, which is consistent with the zeroth law of thermodynamics. Also, Eq. (13) makes condition Eq. (19) satisfied. The boundary condition Eq. (20) can be rewritten in equivalent and more convenient form

$$\tilde{\nu}_{ij} l^a \partial_a n_j = \left(\frac{\partial f_*}{\partial n_i}\right)_{T,n_{j\neq i}}, \tag{21}$$

where $f_* = u_* - Ts_*$ is the surface Helmholtz energy density, and $\tilde{\nu}_{ij} = T\alpha_{ij}$. Equations (17) and (18) with boundary conditions Eq. (21) provide correct problem statement for equilibrium states of the mixture, while Lagrange multipliers λ_0,λ_i must be chosen to supply the fixed quantities Eqs. (7) and (8).

For further analysis, it is convenient to introduce the tensor,

$$\sigma_{ab} = (-p + \kappa_i n_i + 2^{-1}\tilde{\nu}_{ij}\partial_a n_i \partial_a n_j + T\Theta_i n_i)\delta_{ab} - \tilde{\nu}_{ij}\partial_a n_i \partial_b n_j. \tag{22}$$

It will be demonstrated below that this tensor represents the static stresses in the mixture (see also the derivation of this tensor in Refs. [2,9,10]. In a particular case of homogeneous mixture, the tensor in Eq. (22) is reduced to the hydrostatic pressure,

$$\sigma_{ab} = -p\delta_{ab}. \tag{23}$$

Using Eqs. (9)–(11) it is easy to demonstrate the validity of the following identity in general case:

$$\partial_b(T^{-1}\sigma_{ab}) = u\partial_a\Theta_0 + n_i\partial_a\Theta_i. \tag{24}$$

Therefore, when the equilibrium conditions Eqs. (17) and (18) are satisfied, we obtain from Eq. (24) the usual equations for the mechanical equilibrium with external forces:

$$\partial_b\sigma_{ab} = n_i\partial_a\phi_i. \tag{25}$$

Now we consider governing equations for the hydrodynamic problems. We use the classical continuum mechanics set of equations that are local conservation laws for chemical components of the mixture, momentum, and energy, respectively, when there exist external potential forces [45]:

$$\partial_t n_i + \partial_a(n_i v_a + Q_{ia}) = 0, \tag{26}$$

$$\partial_t(\rho v_a) + \partial_b(\rho v_a v_b - p_{ab}) = -n_i\partial_a\phi_i, \tag{27}$$

$$\partial_t\varepsilon + \partial_a(\varepsilon v_a + q_a - p_{ab}v_b) = 0, \tag{28}$$

where p_{ab} is the stress tensor, and q_a is the heat flux inside the mixture. Equation (26) is consistent with mass conservation, because together with the condition in Eq. (2) it produces usual continuity equation

$$\partial_t\rho + \partial_a(\rho v_a) = 0. \tag{29}$$

The boundary conditions at the immobile solid walls include Eq. (21) and the following additional constraints:

$$v_a = 0, \tag{30}$$

$$l^a Q_{ia} = 0, \tag{31}$$

$$\partial_t u_* = l^a\left(q_a^{\text{ext}} - q_a\right), \tag{32}$$

where $q_a^{\rm ext}$ is the external heat flux. Boundary conditions Eqs. (21), (30)–(32) possess clear physical meaning and can be explained in the following way:

(1) Eq. (21) reflects the wetting properties of the boundary ∂D.

(2) Eq. (30) is the usual no-slip condition for the mass velocity. In case of gases, this condition should be substituted with slip condition; however, gas flow is outside the scope of the present paper.

(3) Eq. (31) establishes that the solid surface ∂D is impermeable to the diffusion flux Q_{ia}.

(4) Eq. (32) is the boundary energy conservation law.

Hydrodynamic Eqs. (26)–(28) and boundary conditions Eqs. (21), (30)–(32) form a complete mathematical problem for primary variables n_i, v_a, u. Yet the problem requires additional information to be closed. The hydrodynamic model must be closed by specifying: (a) explicit expressions for the thermodynamic potentials s, u_*, s_* and (b) constitutive relations for the fluxes Q_{ia}, p_{ab}, q_a. The former are determined by the chemistry of the mixture, while the latter should be introduced in accordance with the entropy production principle, which we are to consider presently.

To make mathematical expressions compact it is convenient to introduce additional notations $Q_{0a} \equiv q_a$, $\phi_0 \equiv 0$, and J_{sa}, which is entropy flux. Then, using Eqs. (26)–(28), one can calculate the local entropy production rate χ:

$$\partial_t \theta + \partial_a J_{sa} = \chi, \tag{33}$$

$$J_{sa} = (u\Theta_0 + n_i\Theta_i)v_a - \Sigma_{ab}v_b + Q_{Aa}(\Theta_A - \Theta_0\phi_A) + \alpha_{ij}\partial_t n_i \partial_a n_j, \tag{34}$$

$$\chi = T^{-1}(p_{ab} - \sigma_{ab})\partial_b v_a + Q_{Aa}\partial_a(\Theta_A - \Theta_0\phi_A). \tag{35}$$

Here and below, the indices A, B run through numbers $0, \ldots, M$. As before, the summation is implied over the repeated indices. The canonical form of the entropy Eq. (33) represents the entropy changes caused by both entropy flux and local entropy production [44,46]. At this point, it is time to introduce viscous stress tensor $\tau_{ab} = p_{ab} - \sigma_{ab}$. As one can see from Eq. (35), the tensor σ_{ab} constitutes a part of the total stress tensor p_{ab} that does not affect the entropy production. Also, it does not depend on the velocity v_a, and it is uniquely determined by the instantaneous configuration of the fields n_i, u. This is why σ_{ab} is interpreted as static stress tensor. In order to have consistency with the second law of thermodynamics, the local entropy production rate Eq. (35) must be nonnegative. This can be achieved by using constitutive relations satisfying two independent inequalities:

$$\tau_{ab}\partial_b v_a \geqslant 0, \tag{36}$$

$$Q_{Aa}\partial_a(\Theta_A - \Theta_0\phi_A) \geqslant 0. \tag{37}$$

There are many ways to satisfy these inequalities. Here, we give only the simplest options. For the viscous stress tensor τ_{ab}, one can use the following constitutive relation:

$$\tau_{ab} = \eta_{\rm v}\delta_{ab}\partial_c v_c + \eta_{\rm s}\left(\partial_a v_b + \partial_b v_a - \tfrac{2}{3}\delta_{ab}\partial_c v_c\right), \tag{38}$$

with $\eta_{\rm v}$ and $\eta_{\rm s}$ being nonnegative bulk and shear viscosity coefficients, respectively. In the linear viscous model, these coefficients can depend on local temperature and component densities. In nonlinear viscous models, they can depend also on local velocity gradient. When the liquid is affected by the forces in the close vicinity of the solid surface, $\eta_{\rm v}$ and $\eta_{\rm s}$ can depend on coordinates.

For the fluxes Q_{Aa} one can use the following constitutive relation:

$$Q_{Aa} = \mu_{AB}\partial_a(\Theta_B - \Theta_0\phi_B), \tag{39}$$

with μ_{AB} being a nonnegative definite symmetric matrix with one zero eigenvalue [i.e., to provide consistency with the condition in Eq. (2)]:

$$\mu_{Ai}m_i = 0. \tag{40}$$

The constitutive relations Eqs. (38) and (39) close the hydrodynamic model. To apply this model to the description of particular multiphase flow scenarios, one should specify explicitly the thermodynamic potentials s, u_*, s_* and the transport coefficients in Eqs. (38) and (39). This can be done using experimental data for bulk and surface thermodynamics, thermal and diffusive transport, and viscous stresses. Also, certain interpolation and extrapolation procedures can be used when input data does not cover the entire range of temperature and component density values [2].

Integration of the local entropy Eq. (33) over the whole region D with account of boundary conditions Eqs. (21), (30)–(32) produces the dynamic equation for the total entropy of the mixture:

$$\frac{dS_D}{dt} = \int_{\partial D} l_a T^{-1} q_a^{\rm ext} dA + \Sigma, \tag{41}$$

where Σ is the total entropy production rate, which is nonnegative because of the inequalities (36) and (37); i.e.,

$$\Sigma = \int_D \chi dV \geqslant 0. \tag{42}$$

As one can see from Eqs. (41) and (42), when the external heat flux is nonexistent, $q_a^{\rm ext} \equiv 0$, the entropy of the mixture S_D can only grow in accordance with the second law of thermodynamics.

Now let us consider some applications of the static stress tensor σ_{ab}.

First, this tensor can be used to calculate interfacial tension between fluid phases. Indeed, if we consider an equilibrium 1D solution $T = \text{const}, n_i = n_i(x^1)$ describing the transition from one phase n_{i-} at $x^1 \to -\infty$ to another phase n_{i+} at $x^1 \to +\infty$, then the interfacial tension is calculated by the following procedure [47]:

$$\gamma = \int_{-\infty}^{+\infty} (\sigma_{22} - \sigma_{11})dx^1 = \int_{-\infty}^{+\infty} \tilde{\nu}_{ij}\partial_1 n_i \partial_1 n_j dx^1. \tag{43}$$

This particular equation can be used in numerical modeling to fix the parameters $\tilde{\nu}_{ij}$ from the known parameter γ.

Second, let us consider an equilibrium 1D solution $T = const$, $n_i = n_i(x^1)$ in the vicinity of the solid surface. In accordance with the mechanical equilibrium Eq. (25), here

we have the equation for the static stress component σ_{11}:

$$\partial_1 \sigma_{11} = n_i \partial_1 \phi_i. \tag{44}$$

We consider the situation when there exists a liquid layer of the thickness h in the vicinity of the surface. Farther away is another liquid phase. The aim is to evaluate the so-called disjoining pressure, Π, which is the additional pressure (i.e., in respect to the bulk pressure) in the liquid at the surface [41,42,48]. This disjoining pressure can be positive or negative. By definition, the disjoining pressure is zero for infinite parameter h. After integrating Eq. (44) over the interval $[0, L]$, one can arrive to the following equation:

$$-\sigma_{11}(0) = -\sigma_{11}(L) - \int_0^L n_i \partial_1 \phi_i dx^1. \tag{45}$$

By definition, the hydrostatic pressure in the bulk can be calculated as $p = -\lim_{L\to+\infty} \sigma_{11}(L)$. Therefore, Eq. (45) produces the following relation between the static stress in the liquid at the surface and the bulk pressure:

$$-\sigma_{11}(0) p + \Psi(h),\ \Psi(h) = -\int_0^{+\infty} n_i \partial_1 \phi_i dx^1. \tag{46}$$

Using the definition of the disjoining pressure it is possible to produce the following expression:

$$\Pi(h) = \Psi(h) - \Psi(+\infty). \tag{47}$$

This last expression can be put in a simpler form under the following assumptions:

(a) liquid layer consists only of the component 1 with almost constant density n_{10}, while another liquid contains no component 1;

(b) there is only one nonzero potential $\phi_1 = \phi_1(x^1)$, which vanishes at spatial infinity.

Under these assumptions the expression in Eq. (47) is reduced to the following approximation:

$$\Pi(h) \approx -n_{10} \phi_1(h). \tag{48}$$

These relations can be used to calculate disjoining pressure from the external potential $\phi_1 = \phi_1(x^1)$ and vice versa.

Now it is useful to discuss some simplified cases in DFH. In many instances it is sufficient to perform simulations in isothermal approximation. Isothermal hydrodynamic equations can be derived using nonisothermal equations assuming constant temperature,

$$T = \text{const}, \tag{49}$$

and excluding from consideration the energy Eq. (28) together with boundary condition Eq. (32). In this case, the constitutive relations in Eq. (39) are effectively reduced to a simpler system of equations:

$$Q_{ia} = \mu_{ij} \partial_a (\Theta_i - \Theta_0 \phi_i). \tag{50}$$

It is necessary to note that the isothermal formulation of DFH can also be rigorously built on the Helmholtz energy functional instead of the entropy functional Eq. (5) [2,9]. In order to make this matter clear, we briefly trace here the basic steps of the Helmholtz energy approach. The Helmholtz energy functional, which corresponds to the functional Eqs. (5) and (7), can be represented as follows:

$$F_D = U_D - T S_D = \int_D (f + 2^{-1} \tilde{\nu}_{ij} \partial_a n_i \partial_a n_j + \phi_i n_i) dV + \int_{\partial D} f_* dA, \tag{51}$$

where $f = u - Ts$ is Helmholtz energy density for homogeneous mixture without external potentials.

In isothermal problems, Helmholtz energy functional must be considered as to be dependent on molar density fields n_i, while temperature T is a fixed parameter. Equilibrium states of the mixture correspond to conditional critical points of the functional Eq. (51) under the constraints that amount of components N_{iD} are fixed, i.e.,

$$\delta F_D - \zeta_i \delta N_{iD} = 0, \tag{52}$$

where ζ_i are the Lagrange multipliers. This variational equation leads to the equilibrium conditions, which include equations in the bulk:

$$\Phi_i + \phi_i = \zeta_i, \tag{53}$$

$$\Phi_i = \kappa_i + 2^{-1} \tilde{\nu}_{jk,i} \partial_a n_j \partial_a n_k - \partial_a (\tilde{\nu}_{ij} \partial_a n_j), \tag{54}$$

and the boundary Eq. (21). Evidently, the equilibrium Eq. (53) is equivalent to Eq. (18) together with the condition Eq. (49).

Isothermal DFH is governed by the component and momentum conservation Eqs. (26) and (27) without energy Eq. (28). It is possible to verify that the described system is dissipative. This dissipation property is similar to the nonnegative entropy production in the case of nonisothermal processes. Direct calculation of time derivative of the sum of kinetic and Helmholtz energy with account of the boundary conditions Eqs. (21), (30), and (31) leads to the dissipative function $\tilde{\chi}$ as follows:

$$\frac{d}{dt}\left(2^{-1} \int_D \rho v_a v_a dV + F_D\right) = \int_D \tilde{\chi} dV, \tag{55}$$

$$\tilde{\chi} = Q_{ia} \partial_a (\Phi_i + \phi_i) - \tau_{ab} \partial_a v_b. \tag{56}$$

For isothermal problems, one can represent constitutive relations in Eq. (50) in the following way:

$$Q_{ia} = -D_{ij} \partial_a (\Phi_i + \phi_i), \tag{57}$$

where $D_{ij} = T^{-1} \mu_{ij}$. Now it is easy to see that subject to the constitutive relations Eqs. (38) and (57), we get the inequality $\tilde{\chi} \leqslant 0$, and thus the considered system is dissipative.

In this paper, we consider several applications to isothermal problems, though the existing numerical simulator (Sec. III) can also handle nonisothermal cases. The previous discussion demonstrates that the reduction to isothermal processes is quite consistent with Helmholtz energy theory.

As a conclusion to this section, we put here a brief summary on how various multiphase phenomena are accounted for in the frame of the DFH.

(1) Interfacial tension is taken into account by means of molar density gradient term that enters the expression for entropy Eq. (6). Assuming γ is known from experiment the Eq. (43) is solved numerically to find parameters $\tilde{\nu}_{ij}$.

(2) Adsorption (e.g., surfactants) into interfacial area between mobile liquid phases is incorporated into the theory by the dependence of coefficients α_{ij} in Eq. (6) on local composition.

(3) Wettability (interfacial tension between liquid and solid) and adsorption onto solid boundaries are described by the boundary condition Eq. (21).

(4) Coalescence and breakup of droplets as well as any other topological changes of interfacial boundaries happen naturally and can be traced from evolution of molar density fields.

(5) Motion of interfacial boundary over solid surface (i.e., moving contact line) is possible despite presence of no-slip boundary condition Eq. (30); it is enabled by the nonlinear diffusion fluxes Q_{ia} Eq. (39) that enter the molar density conservation Eq. (26) and can be nonzero over the surface.

(6) DFH is not limited to Newtonian rheology and can handle non-Newtonian rheologies by using appropriate expression for viscous stress tensor instead of the Navier-Stokes's one in Eq. (38). In particular, viscoelastic, viscoelastoplastic, as well as the well-known Herschel-Bulkley rheological models can be employed [1,2].

(7) Phase transitions are governed by the bulk entropy or Helmholtz energy properties following the classical theories [44,49]; their particular expressions should be selected to represent fluid experimental behavior. In the present paper, we used conventional analytical expressions [1,2,13].

(8) Hydrodynamic Eqs. (26)–(28) are solved in each spatial point of a domain containing multicomponent mixture. Accordingly, the evolution of the system is described by the evolution of molar densities of chemical components and mass velocity. For multiphase mixtures, the position of an interface is indicated by high molar density gradients similarly to the so-called "diffuse-interface" methods [37].

(9) There are extensions of DFH published elsewhere [2] that significantly widen the range of phenomena that can be modeled.

III. NUMERICAL EXAMPLES

All the numerical results presented in this section have been produced by solving numerically the equations of the density functional hydrodynamics (DFH) described in Sec. II. The numerical simulations have been carried out by the computer code called direct hydrodynamic (DHD) simulator. This simulator, as a fully parallel code, was developed by Schlumberger Moscow Research (SMR) in 2005; however, the rudimentary serial versions of the code were created by the authors in early 2000s. In 2009–2011, the code was optimized for running on multi-GPU clusters. This has enabled a 30- to 40-fold increase in performance in comparison with the previous version designed for CPU clusters. Simulation experience accumulated over the past several years yielded that depending on the physics of the multiphase problem the typical scenarios can be simulated on models with sizes from 200^3 cells (on several GPU cards) to 1000^3 cells (on a 64-GPU cluster) within a day. To enable modeling of the examples described in this section, the simulator has been updated.

As it was explained in Sec. II, the endowing of DFH with the necessary liquid nanoflow phenomena description was achieved through introduction of external potentials. From the numerical simulation point of view, those potentials serve as a convenient way to unlock the required modeling capabilities using the relatively simple implementation within the existing code. The required implemented modifications encompass the right part in Eq. (27); the new term with ϕ_i in the constitutive relation Eq. (39); procedures for calculation of the potentials themselves; and the results post-processing in terms of the disjoining pressure as specified in Eqs. (45)–(48). These important modifications did not influence in any way the already verified existing functionality of the DHD code.

Here we put a brief summary about the DHD. The DHD code solves numerically the dynamic equations of the DFH, namely Eqs. (26)–(28), with boundary conditions Eqs. (21), (30)–(32). The code uses an explicit conservative uniform finite volume numerical scheme on a staggered grid. The numerical method possesses first-order approximation in time and second order in space. A particular numerical scheme implemented in DHD was specifically designed to accommodate for the DFH equations. The scheme is called tensor-aligned conservative uniform scheme on a staggered grid (TACUS); its description can be found in Ref. [2]. A detailed description and analysis of numerical methods belonging to the same class can be found, for example, in Refs. [50,51]. To date, DHD simulator has been extensively verified by a lot of numerical exercises, such as standard grid convergence tests [2], various single-phase, two-phase, and three-phase problems that have analytical solutions [1,2]. The simulator capabilities were demonstrated by solving various multiphase problems with complex physics (non-Newtonian rheology, phase transitions, presence of surfactants, mobile solid phase, turbulence, thermal effects) [1,2,15]. Recently, we also demonstrated additional verification of the DHD simulator in respect to typical two-phase pore-scale phenomena inherent to porous media flow [11–13]; those studies include comparison between numerical simulation and experimental results.

In this section, we review numerical simulation examples related to nanoscale compositional fluid systems. Each of the demonstrated examples highlights specific nanoscale phenomenon important in compositional fluid applications, in particular:

(1) Disjoining pressure (Sec. III A),

(2) Film precursors and anomalous rheology (Sec. III B),

(3) Compositional fluid in contact with heterogeneous surface (Sec. III C),

(4) Capillary condensation (Sec. III D),

(5) Forward and reverse osmosis (Sec. III E).

The numerical examples presented here demonstrate possibilities of the DFH in nanoscale modeling and are not intended for a quantitative validation of the numerical method. Such validation was among the subjects of our previous publications referenced above.

In numerical modeling, we generally rely on the expressions for Helmholtz energy density $f = f(T,n_i)$ obtained using equation of state approach [52]. But in many practical cases, to speed up computations, we use rational approximations for f wherever possible; see the Appendix. Also, in some problems, we use Helmholtz energy approximations, which are compatible with the assumption of 100% pure phase. But,

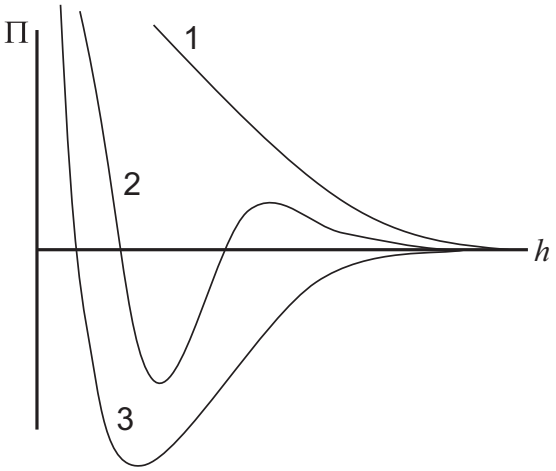

FIG. 1. Schematic representation of disjoining pressure (Π) isotherms corresponding to different wetting scenarios: (1) complete wetting, (2) partial wetting, (3) nonwetting.

because of diffuse interface approach, pure composition is never actually realized in multiphase numerical simulations.

A. Disjoining pressure

An important phenomenon observed near submicron scale at liquid-surface contact is possible thermodynamically stable coexistence of both liquid film and bulk liquid belonging to the same phase in proximity of the liquid drop [41,42,48,53–55]. Some publications utilize different terminology where the film and the bulk fluids are named as separate thermodynamically dissimilar phases [56]. Importantly, the bulk fluid have specific equilibrium contact angle over the film depending on the properties of the fluid and the surface. The conventional surface chemical explanation of this phenomenon is based on the concept of disjoining pressure that was introduced by Derjaguin in 1936 [41]. The nature of the disjoining pressure can be understood on the level of molecular layers and orientation of the molecules as explained in terms of interactions often grouped under the general name of van der Waals forces [57,58]. In continuum class models (DFH belongs to this class), description of the disjoining pressure can be introduced using the idea of the disjoining pressure isotherm [42].

Dynamic phenomena such as spreading thin liquid layers with account for evaporation and condensation can be modeled using phase field theory with disjoining potential (i.e., quantity conjugated to disjoining pressure) as demonstrated by Pismen and Pomeau [59] for a single component fluid. The density functional theory can be used to calculate disjoining pressure or potential of a single component fluid in a straightforward manner as presented by Henderson [56]. Our DFH modeling technique described in Sec. II can be considered as a further generalization of these ideas in nanoscale dynamic phenomena modeling for compositional mixtures.

Disjoining pressure isotherms are based on experimental data and can describe different possible wetting scenarios as shown schematically in Fig. 1 [42].

In DFH, we use the concept of the disjoining potential, which is directly related to the disjoining pressure by Eqs. (45)–(48) (in Sec. II a general term "external potential" is used). To demonstrate consistency of our modeling, we present three numerical simulation examples corresponding to different wetting scenarios: Case 1, complete wetting; Case 2, partial wetting; and Case 3, nonwetting. In each case, we use the same parallelepiped model geometry with dimensions 200 nm × 200 nm × 80 nm discretized using 200 × 200 × 80 grid with identical cubic cells.

The numerical simulations for all cases listed in this section were performed using the same pair of fluids with the following properties: $\rho_A = 1000\,\mathrm{kg/m^3}$, $\rho_B = 800\,\mathrm{kg/m^3}$, $m_1 = 18\,\mathrm{kg/kmol}$, $m_2 = 100\,\mathrm{kg/kmol}$, $\eta_A = 0.001\,\mathrm{Pa\cdot s}$, $\eta_B = 0.002\,\mathrm{Pa\cdot s}$, and $\gamma_{AB} = 0.022\,\mathrm{N/m}$, where ρ_A, ρ_B are mass densities of phases A and B; m_1,m_2 are molar masses of components 1 and 2; η_A, η_B are shear viscosities of phases A and B; and γ_{AB} is interfacial tension. The phases are defined in such a way that phase A consists 100% of component 1, while phase B consists 100% of component 2.

The initial and boundary conditions are the same in all simulated cases. The model has periodic boundary conditions in lateral directions (i.e., x and y), which makes numerical simulations physically consistent. In vertical direction (i.e., z), the model has impermeable boundaries. For the most part of the volume, the model is filled with phase A. Immediately adjacent to the bottom side of the model (i.e., at $z = 0$) and at its geometrical center, a parallelepiped-shaped fragment of phase B is placed; the sizes of the fragment are 96 nm × 96 nm × 50 nm [Fig. 3(a)].

The three simulated cases are different in the shape of the disjoining potential, which is a function of the vertical coordinate, i.e., distance from the surface, $\phi_2 = \phi_2(z)$ [Fig. 2(a)]. The lower index 2 indicates that the potential is related to the second chemical component constituting phase B. The model function ϕ_2 depicted in Fig. 2(a) was taken as follows:

$$\phi_2(z) = (a_1 z^2 + a_2 z + a_3)\,\exp(-a_4 z^2). \tag{58}$$

The values of model parameters a_1,a_2,a_3,a_4 used in the numerical simulations are listed in Table I.

The numerical simulation results showing equilibrium distribution of phases are presented in Figs. 3(b) and 3(c). Figure 2(b) shows equilibrium disjoining pressure profiles for each of the simulated cases. The profile is taken at the center of the model and along z axis. As expected, in Case 1 [Fig. 3(b)], the initial nonequilibrium fragment of phase B has evolved to a uniform film that evenly covers the entire bottom surface of the model. In Case 2 [Fig. 3(c)], the system has evolved to the state in which there is still a film covering the entire bottom of the model, but unlike Case 1, equilibrium thickness of the film

TABLE I. Scope of the disjoining potential model parameters.

	$a_1(\mathrm{N\,m^{-1}kmol^{-1}})$	$a_2(\mathrm{N\,kmol^{-1}})$	$a_3(\mathrm{N\,m\,kmol^{-1}})$	$a_4(\mathrm{m^{-2}})$
Case 1	-4.62×10^{20}	1.76×10^{13}	-2.25×10^{5}	5×10^{5}
Case 2	-2.43×10^{21}	7.29×10^{13}	-3.04×10^{5}	8×10^{5}
Case 3	-4.53×10^{21}	8.66×10^{13}	-3.2×10^{5}	10^{16}

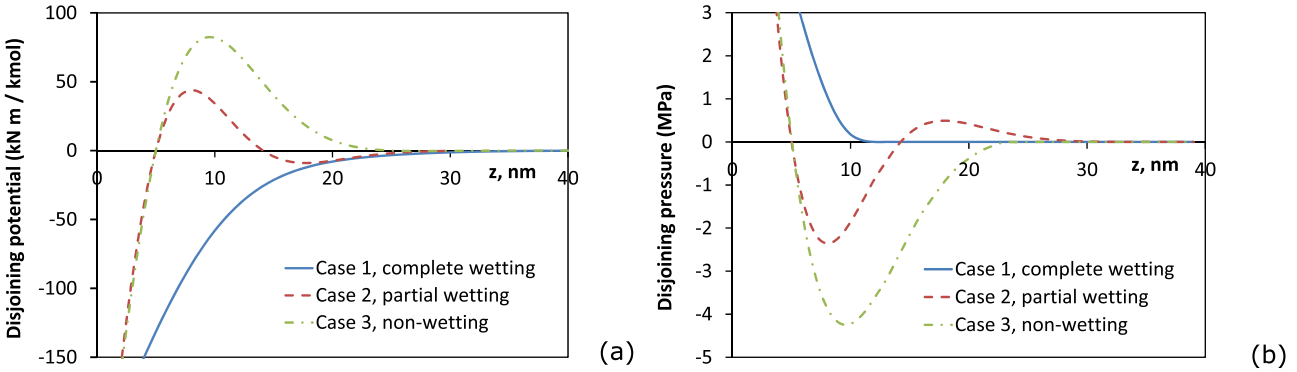

FIG. 2. (a) Disjoining potentials used in the numerical modeling of the different wetting scenarios. (b) Disjoining pressure profile obtained in the equilibrium numerical solution for the different wetting scenarios; the profile is taken at the center of the model and along the z axis.

in Case 2 is limited by the disjoining potential, which becomes positive at approximately 6-nm distance from the surface. At farther distance, the film becomes unstable and excessive amount of phase B bulks in a shape of a droplet. In Case 3 [Fig. 3(d)], the equilibrium film thickness is the same as in Case 2, but because disjoining potential has larger positive range, the droplet has evolved to a different shape, which is characteristic for nonwetting fluids. This result has particular importance as it demonstrates direct modeling of the phenomenon that can be considered paradoxical at the first glance: a simultaneous presence of the localized nonwettability and the film.

The solutions shown in Figs. 3(b) and 3(c) cannot be realized in conventional DFH modeling shown in our previous publications, where the concept of the disjoining potential was not present. Before the DFH extension developed in this paper, both wettability and adsorption were governed by the boundary condition Eq. (21) alone. Therefore, only two scenarios could be modeled by the previously published model: Either a complete wetting where the entire volume of wetting phase spreads over the surface and forms film of arbitrary thickness, or wetting with certain contact angle; but in the latter case the film could not exist. The concept of the disjoining potential introduced in the new DFH model described in Sec. II eliminates this limitation of the previous model as was demonstrated in this section.

B. Film precursors and anomalous rheology

In Sec. III A, we did not focus on the dynamic effects that can take place during the evolution to the equilibrium solutions like those shown in Figs. 3(b)–3(d). However, there are important dynamic phenomena inherent in the nanoscale fluid systems. These phenomena include existence of film precursors [53,54] and anomalous rheology of the films [60]. Film precursors are distinguished from the equilibrium films, because the former is essentially dynamic phenomenon. In DFH modeling of spreading dynamics, one can observe film precursors, as will be demonstrated further in this section.

Another observation related to thin films (i.e., in case of simple liquids films are considered thin when having thickness on the order of ∼10 nm and less) is that the film rheology is usually considerably different from that of the bulk liquid [60].

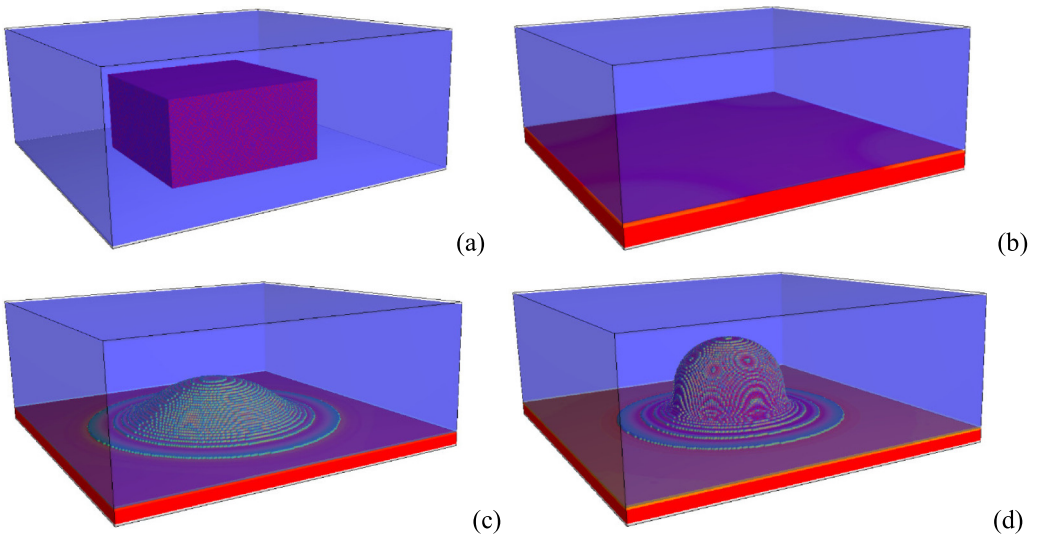

FIG. 3. Initial condition (a). Equilibrium distribution of phases in the numerical solution for (b) Case 1 (complete wetting), (c) Case 2 (partial wetting), and (d) Case 3 (nonwetting). The images show 3D view of the distribution of phases; phase A is shown in semitransparent blue (light gray) and phase B is shown in red (dark gray), other colors (shades of gray) indicate transition zone.

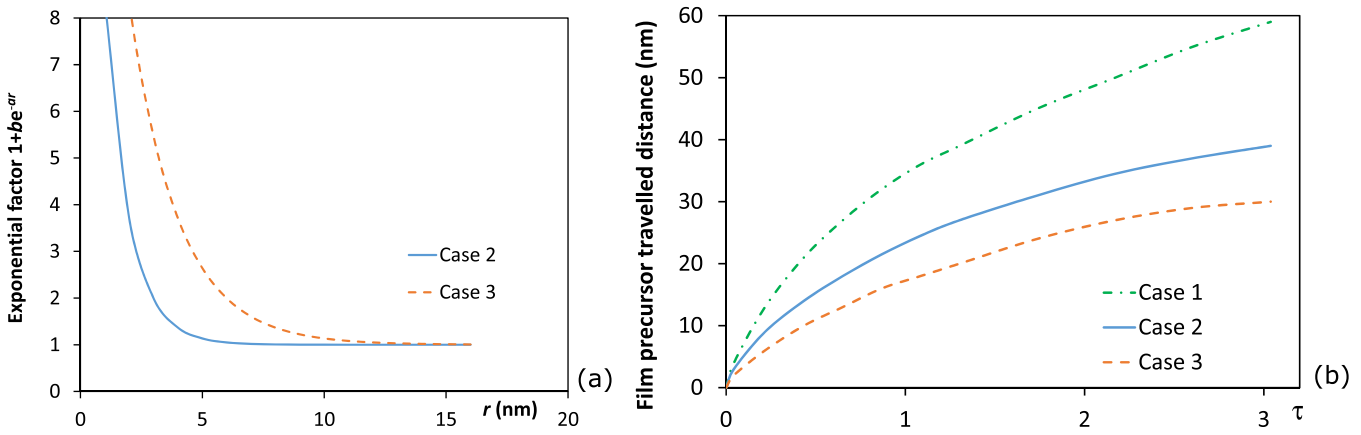

FIG. 4. (a) Exponential factor $1 + be^{-a\,r}$ in the effective viscosity model in Eq. (59) showing deviation between the bulk and the thin film theology in Cases 2 and 3. (b) Film precursor travelled distance as a function of the dimensionless time (τ) as obtained in the numerical simulations.

Thin films demonstrate dramatic growth of effective viscosity as approaching the surface. In addition, they demonstrate pronounced non-Newtonian behavior, e.g., dependence of effective viscosity on shear rate. These rheological features are captured by DFH modeling.

Numerical simulation presented here was performed on a parallelepiped model with dimensions 240 nm × 240 nm × 80 nm discretized using 240 × 240 × 80 grid with identical cubic cells.

The model has periodic boundary conditions in lateral directions. In vertical direction, it has impermeable boundaries. Initial conditions were similar to those of Sec. III A [Fig. 3(a)]. The disjoining potential $\phi_2 = \phi_2(z)$ was taken from Case 3 of Sec. III A [Fig. 2(a)].

Three scenarios were simulated numerically. In the first scenario (Case 1), there was no difference in rheology between bulk and film liquids. In the two other scenarios, the rheology of phase B was described by the effective viscosity model as follows:

$$\eta_{\mathrm{B}}^{\mathrm{eff}} = \eta_{\mathrm{B}}(1 + b\,e^{-a\,r}), \tag{59}$$

where r is distance to solid surface, a,b are positive model parameters. The model Eq. (59) ensures exponential growth in effective viscosity of the film with approach to the surface following the qualitative trend described in Ref. [60], pp. 580–591. In the numerical simulations presented here we used $a = 10^9\ \mathrm{m}^{-1}$ for Case 2 and $a = 5 \times 10^{10}\ \mathrm{m}^{-1}$ for Case 3, while parameter b was the same in these both cases, $b = 20$ [Fig. 4(a)]. As can be seen from Fig. 4, considerable deviation between bulk and film rheology occurs at about $r < 5$ nm in Case 2 and much earlier, at about $r < 10$ nm, in Case 3.

Results of the numerical simulation by DFH are presented in Figs. 4(b) and 5. Particularly, Fig. 4(b) shows the distance travelled by the film precursor as a function of dimensionless time τ defined by $\tau = t\,L^{-2}\rho_{\mathrm{B}}^{-1}\eta_{\mathrm{B}}$, where t is time and L is the reference size of the model. As expected, the film precursor propagates considerably slower when anomalous rheology of the film is accounted. Figure 5 demonstrates distribution of phases for each of the cases captured at the same dimensionless time $\tau = 3.04$.

C. Compositional fluid in contact with heterogeneous surface

In the two previous sections, we dealt with the ideal systems having a flat solid surface and a simple two-phase, two-component mixture. However, majority of natural surfaces exhibit certain extent of heterogeneity in distribution of properties (e.g., wettability, adsorptivity). Generally, the heterogeneity can be attributed to variability in composition, surface contamination, or geometrical defects. Even artificial surfaces prepared in strictly controlled laboratory conditions cannot be completely devoid of heterogeneity.

Another complication comes from the fact that most natural fluids are compositional, meaning that they consist of many different chemical components. For example, natural hydrocarbon fluids may contain hundreds and thousands of components [61]. Consequently, homogeneous phases have complex composition. Each component has individual

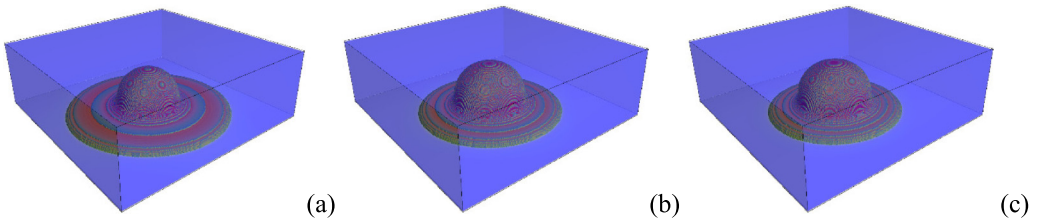

FIG. 5. A single scene from the numerical solution for (a) Case 1, (b) Case 2, and (c) Case 3. The scene corresponds to the same dimensionless time $\tau = 3.04$. The images are 3D views showing distribution of phases, where phase A is shown in semitransparent blue (light gray) and phase B is shown in red (dark gray); other colors (shades of gray) indicate transition zone.

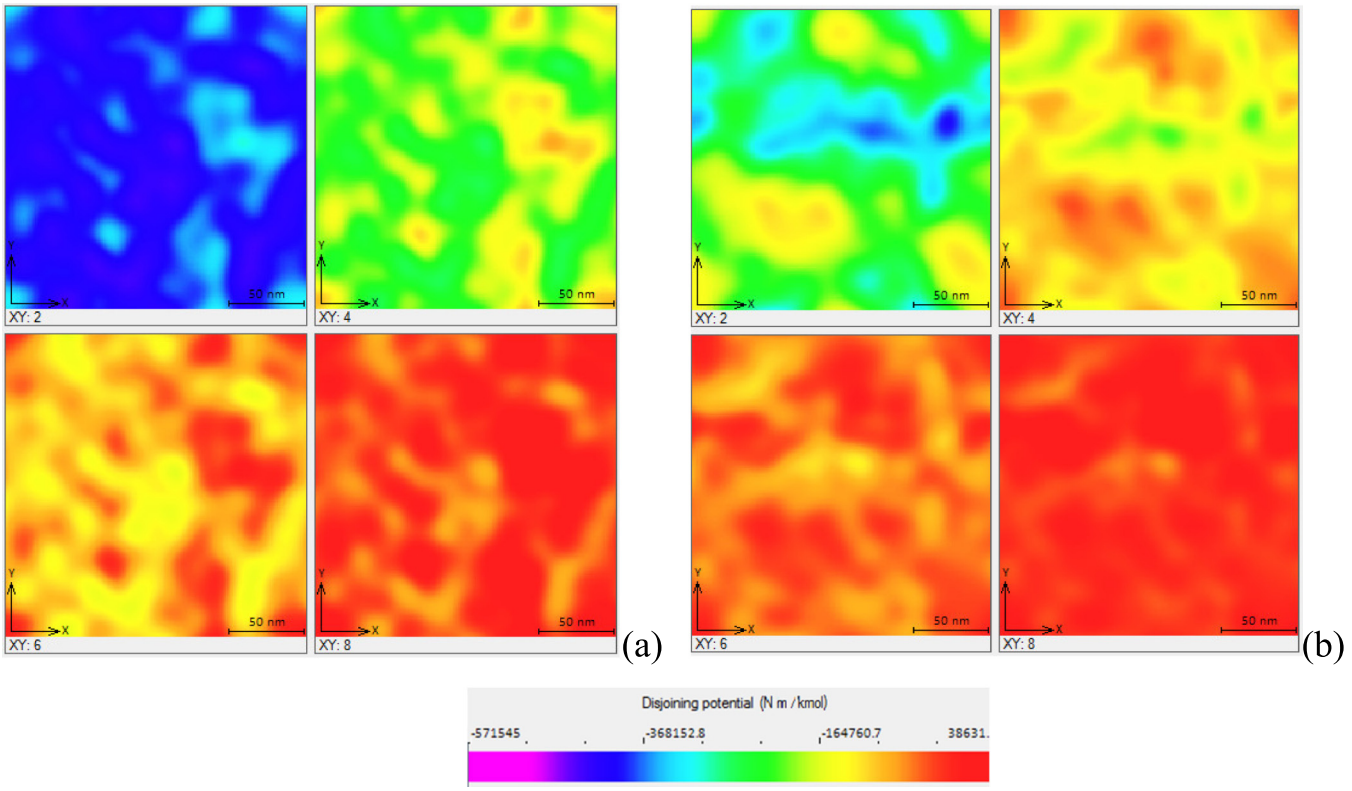

FIG. 6. Disjoining potentials distribution for component 2 (a) and component 3 (b) as seen in 2D cross-sections of the 3D model taken parallel to the xy plane at distance of 1 nm, 3 nm, 5 nm, and 7 nm (left-right, top-bottom) counted from the bottom of the model. Colors indicate disjoining potential values (N m kmol^{-1}) according to the color palette.

properties characterizing its interaction with solid surfaces. For example, two component phases may wet a surface; but one of the components may wet the surface better than the other. This results in composition gradient near the surface. Another possible scenario is when one of the components can be significantly affected by certain surface inhomogeneity types (e.g., adsorb upon certain impurities), while the other component is much less sensitive to those types of inhomogeneity. The processes related to the described phenomena are often referred to as competitive or selective (the latter term refers to the scenario when there is full separation of adsorbates) adsorption [62,63]. Selective and competitive adsorption play important role in many scientific and technological applications dealing with compositional fluids, e.g., chromatography, separation and purification processes, and also in biology.

To model the above said phenomena by DFH, it is necessary to introduce disjoining potentials that are functions of not only the vertical coordinate but of the lateral coordinates as well, $\phi = \phi(x,y,z)$. In addition, while it was sufficient to have just one potential in two-component mixture of Sec. III A, there should be more than one potential for the compositional mixture.

For a modeling example, we consider a mixture that is two-phase, three-component with 100% of component 1 constituting phase A and components 2 and 3 constituting phase B in such a way that they can be mixed in any proportion providing their total molar concentration is unity within phase B, i.e., $c_2 + c_3 = 1$ always holds, where c_2, c_3 are molar concentrations of components 2 and 3. The relevant properties of phases and components are the following: $\rho_A = 1000\,\mathrm{kg/m^3}$, $\rho_2 = 800\,\mathrm{kg/m^3}$, $\rho_3 = 900\,\mathrm{kg/m^3}$, $m_1 = 18\,\mathrm{kg/kmol}$, $m_2 = 100\,\mathrm{kg/kmol}$, $m_3 = 60\,\mathrm{kg/kmol}$, $\eta_A = 0.001\ \mathrm{Pa \cdot s}$, $\eta_B = 0.002\,\mathrm{Pa \cdot s}$, and $\gamma_{AB} = 0.02\,\mathrm{N/m}$, where ρ_A is mass density of phase A; ρ_2, ρ_3 are mass densities of components 2 and 3 for pure substances; m_1, m_2, m_3 are molar masses of components 1, 2, and 3; η_A, η_B are shear viscosities of phases A and B; and γ_{AB} is interfacial tension. The model is parallelepiped with dimensions 250 nm × 250 nm × 80 nm discretized using 250 × 250 × 80 grid. The model has periodic boundary conditions in lateral directions. In vertical direction it has impermeable boundaries. Initially, the model was filled with 100% of phase A.

Disjoining potentials were introduced for components 2 and 3 and both follow the nonwetting trend. Namely, the potentials are negative near the bottom side of the model and positive farther from it, thus providing favorable conditions for a finite thickness thin film and bulk phase at places where thin film exceeds equilibrium thickness (i.e., similar to the trend of Case 3 from Sec. III A). However, due to the spatial variability introduced in ϕ, the conditions are nonuniform leading to variable thickness of the equilibrium film. Practically, the potentials shown in Fig. 6 have been constructed using Eq. (58) as a function of the vertical coordinate z with parameters as in Case 3 from Sec. III A; then, this function has been multiplied by a 3D homogeneous Gaussian random function with the correlation radius equal to 40 nm and the standard deviation equal to 0.3. The difference in the two potentials has been obtained by using two different realizations of the Gaussian

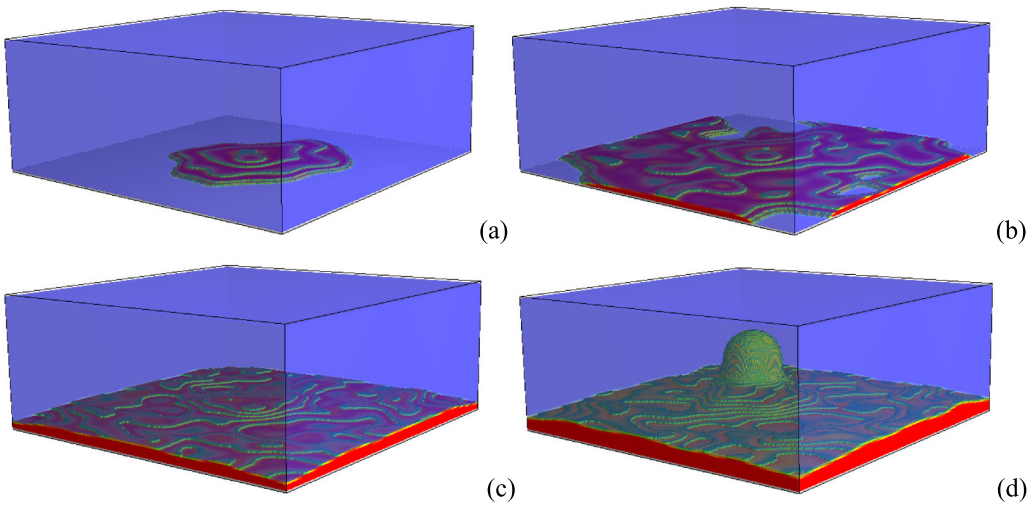

FIG. 7. Numerical simulation results in the model with heterogeneous bottom surface properties. Separate images (a) through (d) show 3D view of consecutive states of the system. Phase A is shown in semitransparent blue (light gray) and phase B is shown in red (dark gray); other colors (shades of gray) indicate transition zone.

distribution, which was also zero centered for component 2 and centered at 0.2 for component 3 (Fig. 6).

During simulation, phase B, formed by 50% of component 2 and 50% of component 3 (molar percentage), was continuously injected with low rate into the model at one point in the geometric center of the bottom side of the model. To sustain material balance, residual fluids were removed at the top side of the model with the rate equal to the injection rate.

Results of the numerical simulation by DFH are presented in Fig. 7. Soon after injection is started, fluid of phase B forms a spill with irregular pattern [Fig. 7(a)]. The irregular shape is explained by the heterogeneity in the disjoining potential used in the simulation (Fig. 6). With more phase B injected the spill grows [Fig. 7(b)] until the entire surface is covered [Fig. 7(c)]. The thickness of phase B's film is nonuniform following the heterogeneity in the disjoining potential. In the course of the continued injection, the film grows until it reaches equilibrium thickness. Then, responding to the extra phase B fluid arriving and film thickness going above equilibrium thickness, the film starts bulging [Fig. 7(d)] and forming bulk phase, which is more energy favorable than film at places far enough (i.e., above film at equilibrium thickness) from the bottom of the model. A bulge grows to a drop absorbing the extra fluid. Thus, at this stage the system arrives to a state in which it has both film and bulk fluid belonging to the same phase. Qualitatively, this solution is similar to that of Case 3 of Sec. III A, but it was reached from different initial condition and with heterogeneous properties of the solid surface. Also, there is a composition gradient within phase B that is evident from Fig. 8, demonstrating distribution of components 2 and 3 related to the state shown in Fig. 7(d). While phase B forms a perfectly continuous cluster, the components 2 and 3 within it are distributed essentially nonuniformly following the pattern contained in corresponding disjoining potentials.

D. Capillary condensation

Another phenomenon observed in nanoscale fluid systems is capillary condensation that occurs in small cracks and pores in thermodynamic conditions below the vapor pressure, so that the condensed liquid is unstable in the bulk. The necessary conditions for this phenomenon require that the surface is wetted by the liquid, and the pore system possesses sufficiently large specific surface. More generally, the capillary condensation means the appearance of the new fluid phase in capillaries and pores, which is thermodynamically unstable in the bulk but

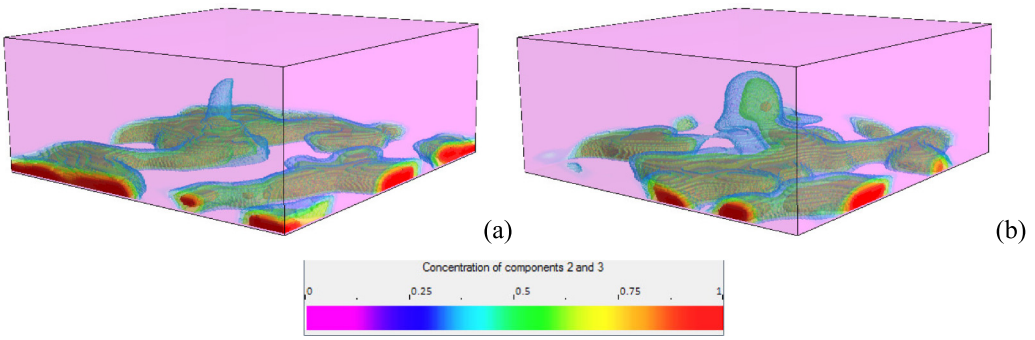

FIG. 8. Numerical simulation results in the model with heterogeneous bottom surface properties. 3D view of (a) component 2 concentration, (b) component 3 concentration. Concentrations are colored according to the color palette. The range [0; 0.4] is semitransparent.

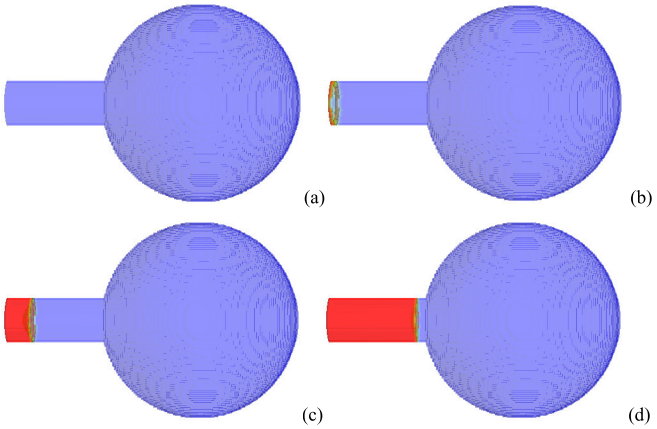

FIG. 9. Numerical simulation results of two-phase capillary condensation in the closed pore system. Separate images (a) through (d) show 3D view of consecutive states of the system. Phase A is shown in semitransparent blue (light gray) and phase B is shown in semitransparent red (dark gray); other colors (shades of gray) indicate transition zone.

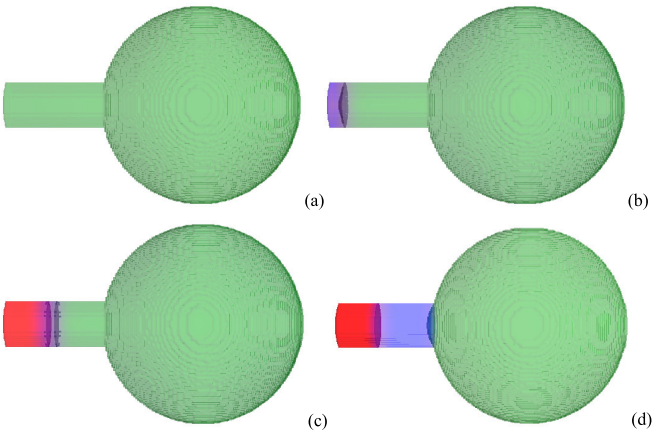

FIG. 10. Numerical simulation results of three-phase capillary condensation in the closed pore system. Separate images (a) through (d) show 3D view of consecutive states of the system. Phases A, B, and C are shown in semitransparent red, green, and blue, respectively.

is favored by specific thermodynamic and wetting conditions in restricted geometry. This phenomenon is important because it may affect greatly properties of materials such powders, membranes, and even rocks making the properties dependent on relative humidity. Capillary condensation has been a subject of study for many years and its description can be found in many books; see, e.g., Refs. [57,64–66]. However, an easy quantitative description based on the well-known Kelvin equation is only possible for the simplest case of two-phase, one-component fluids such as liquid water and water vapor. No such description exists for more complex cases involving compositional fluids and more than two phases, therefore, numerical simulation is required. Here we demonstrate that capillary condensation in complex fluid systems can be directly modeled by DFH.

1. Two-phase mixture

We begin with the case of two-phase, two-component mixture with the same properties as in Sec. III A. The mixture, containing 95% of component 1 and 5% of component 2 (at this composition the mixture is thermodynamically stable in the bulk), is put into a closed pore system consisting of a large spherical pore with radius 50 nm and a thin capillary with radius 12 nm and length 50 nm (Fig. 9). To make this geometry convenient for numerical simulation, the whole figure was inscribed into parallelepiped with dimensions $150\,\text{nm} \times 101\,\text{nm} \times 101\,\text{nm}$ discretized using $150 \times 101 \times 101$ grid. The cells within the parallelepiped, but outside the pore system were made solid (impermeable). The disjoining potential of the second component, $\phi_2 = \phi_2(r)$, was the function of the distance, r, to the solid walls and was calculated using Eq. (58) with parameters of Case 1 from Sec. III A; thus, the walls of the model were wetted by phase B.

Results of the numerical simulation are presented in Fig. 9. Initially, there is no condensate in the model [Fig. 9(a)] as component 2 is completely dissolved in phase A. Figure 9(b) shows that condensation begins in the corners at the end of the thin capillary where the curvature is highest. Then the condensate accumulates gradually with forming meniscus [Fig. 9(c)]; the accumulation continues until the system reaches the equilibrium [Fig. 9(d)].

2. Three-phase mixture

A similar simulation is possible for the three-phase, three-component mixture. For this simulation we used the mixture with properties as follows: $\rho_A = 1000\,\text{kg/m}^3$, $\rho_B = 800\,\text{kg/m}^3$, $\rho_C = 920\,\text{kg/m}^3$, $m_1 = 18\,\text{kg/kmol}$, $m_2 = 100\,\text{kg/kmol}$, $m_3 = 80\,\text{kg/kmol}$, $\eta_A = 0.001\,\text{Pa}\cdot\text{s}$, $\eta_B = 0.002\,\text{Pa}\cdot\text{s}$, $\eta_C = 0.003\,\text{Pa}\cdot\text{s}$, $\gamma_{AB} = 0.02\,\text{N/m}$, $\gamma_{BC} = 0.01\,\text{N/m}$, and $\gamma_{CA} = 0.015\,\text{N/m}$, where ρ_A, ρ_B,ρ_C are mass densities of phases A, B, and C; m_1,m_2,m_3 are molar masses of components 1, 2, and 3; η_A, η_B, η_C are shear viscosities of phases A, B, and C; and γ_{AB}, γ_{BC}, γ_{CA} are interfacial tensions between pairs of phases A-B, B-C, and C-A, respectively. The phases are defined in such a way that phase A consisted of 100% of component 1, phase B consisted 100% of component 2, and phase C consisted 100% of component 3.

The model geometry used here was the same closed-pore system that was employed in the previous two-phase scenario. Also, similar to the previous case, the disjoining potential was the function of the distance to the solid walls and was calculated using Eq. (58) with parameters of Case 1 from Sec. III A. However, now the potential was assigned to two components, 1 and 3, thus the walls of the model could be wet by phases A and C.

Initially, the entire model was filled with uniform thermodynamically stable in the bulk mixture containing 2% of component 1, 95% of component 2, and 3% of component 3, so that components 1 and 3 are dissolved in phase B [Fig. 10(a)]. Results of the numerical simulation are presented in Figs. 10(b)–10(d). Similar to the two-phase scenario, condensation begins in the corners at the end of the thin capillary where the curvature is highest. At the very initial stage, condensation produces a mixture of components 1 and 3 that is not yet split into phases [Fig. 10(b)]. Indeed, suppose that a very small volume vessel contains immiscible components

mixed on the molecular level. Compare it with another vessel of the same volume containing the same mixture, but having equilibrium phases separated. The total energy of the mixture in the second vessel, which is a combination of the bulk energy of the two phases and the energy of the interfacial surface may appear bigger that the energy of the thermodynamically nonequilibrium mixture in the first vessel due to the energy excess produced by the interfacial surface. And it is only with the growth in the volumes that the gain in total energy produced by the interfacial surface can be compensated by the bulk energy loss obtained through phases' separation. A similar effect is known to prevent nucleation of droplets or bubbles with radius below the so-called critical radius, which lies generally below 10÷100 nm [67].

Further in the simulation, the volume of the condensate gradually increases and phases A and C separate [Fig. 10(c)]. Phase A appears at the bottom of the capillary and phase C accumulates in between phases A and B. This configuration is explained by the actual selection of the interfacial tensions that in our case gives $\gamma_{BC} < \gamma_{CA} < \gamma_{AB}$, while the disjoining potentials are the same for phases A and C. This means that it is more energy favorable for phase C, rather than phase A, to appear in contact with phase B. The last image, Fig. 10(d), shows the equilibrium configuration.

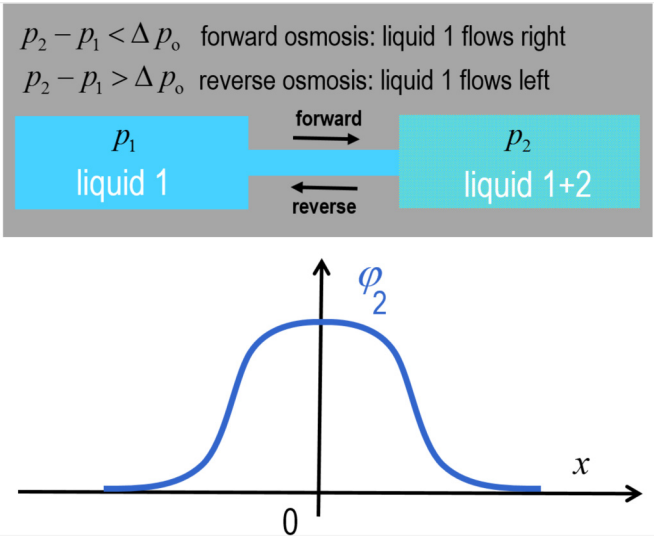

FIG. 11. Schematic representation of size exclusion potential for case of nanoscale channel with constriction. Liquid 1 flow occurs from left to right when $p_2 - p_1 < \Delta p_o$ (forward osmosis) and from right to left when $p_2 - p_1 > \Delta p_o$ (reverse osmosis). Liquid 2 never crosses the constriction.

E. Forward and reverse osmosis

An important factor in nanoscale compositional flow is a possible presence of size exclusion effects when bigger molecules cannot pass constrictions while smaller ones can. This phenomenon is directly related to osmosis, in which a semipermeable membrane is impermeable for solute but not for solvent [66,68]. It is conventional to distinguish between forward and reverse osmosis. Forward osmosis is the process in which solvent penetrates semipermeable membrane separating two closed vessels until pressure difference between the destination and the source vessel raises to osmotic pressure; the latter is consequently defined as the pressure needed to stop forward osmosis. Reverse osmosis is the processes going in reverse direction in respect to forward osmosis and starting when the described above pressure difference is above osmotic pressure (naturally, this situation is only possible after liquid injection to one of the vessels). In either case, the flow is diffusive and is driven by gradients in chemical potentials of the mixture components. It is necessary to stress that when an equilibrium state is reached, i.e., chemical potentials at either side of the membrane became equal, pressures on either side of the membrane are not equal.

In addition to size exclusion, there are other possible mechanisms involved in osmosis, e.g., electromagnetic field influencing mobility of ions and effects related to temperature gradients. In the numerical modeling examples presented here, we focus on the size-exclusion mechanism.

In a continuum mechanics-based method such as the DFH, both forward and reverse osmosis can be modeled by introducing size-exclusion potentials as functions dependent on local geometry. Such potentials can prevent certain chemical components from passing through specific types of geometrical elements. The schematic picture in Fig. 11 explains this idea. The depicted size exclusion potential acts on component 2 of a two-component liquid and prevents this component from passing through the constriction; the solvent (component 1) can pass the constriction freely. The flow of component 1 will occur from left to right when pressure difference between pressure in the right chamber (p_2) and the left chamber (p_1) is still smaller than the osmotic pressure ($\Delta p_o > 0$), i.e., $p_2 - p_1 < \Delta p_o$; thus, this process, forward osmosis, happens along pressure gradient. When $p_2 - p_1 > \Delta p_o$, meaning that pressure difference between the two chambers overcome the osmotic pressure, liquid 1 flows from right to left (reverse osmosis).

Numerical simulation of the forward and reverse osmosis was carried out in the model geometry, consisting of three identical spherical pores having radius of 40 nm and connected together with constricted circular channels. Specifically, the central pore is connected to the left one with the channel having the minimal diameter of 26 nm, while to the right pore it is connected with the thinner channel constricted down to 10 nm diameter [Fig. 12(a)]. For numerical simulation, the model was inscribed into parallelepiped with dimensions 320 nm × 81 nm × 81 nm discretized using 320 × 81 × 81 grid. We used single-phase, two-component liquid mixture with parameters as follows: $\rho_1 = 1000\,\mathrm{kg/m^3}$, $m_1 = 18\,\mathrm{kg/kmol}$, $\rho_2 = 820\,\mathrm{kg/m^3}$, $m_2 = 150\,\mathrm{kg/kmol}$, and $\eta = 0.001\,\mathrm{Pa \cdot s}$, where ρ_1, ρ_2 are mass densities of components 1 and 2 for pure substance; m_1, m_2 are molar masses of components 1 and 2; and η is shear viscosity. The size-exclusion potential acted on the component 2 and was taken in the form of Eq. (58), which was treated as a function of the distance to the walls of the model, with parameters as follows: $a_1 = 0$, $a_2 = -4.8 \times 10^{13}\,\mathrm{N\,kmol^{-1}}$, $a_3 = 1.46 \times 10^5\,\mathrm{N\,m\,kmol^{-1}}$, and $a_4 = 1.5 \times 10^{17}\,\mathrm{m^{-2}}$. The 3D distribution of this size-exclusion potential is presented in Fig. 12(b). The potential vanishes closer to the center of the wider channel, while in the narrower channel

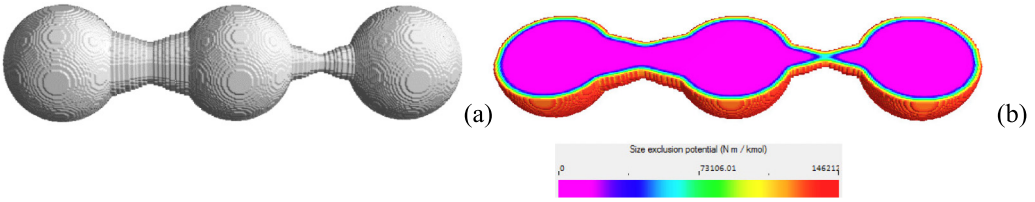

FIG. 12. 3D view of the model geometry (a) and 3D view in cross-section (b) of the size-exclusion potential distribution for forward and reverse osmosis modeling. The potential values (N m kmol^{-1}) are shown according to the color palette.

the potential remains considerable everywhere to prevent component 2 from crossing.

To model forward osmosis we used the problem statement as follows. The central spherical pore of the model was filled with the uniform mixture of two components containing 90% (molar) of component 1 and 10% (molar) of component 2; the rest of the model was filled with 100% of component 1 [Figs. 13(a) and 13(c)]. This distribution corresponded to a constant pressure throughout the model [Fig. 13(e)]. Still, the distribution is nonequilibrium in respect to chemical potentials.

The numerical simulation was carried out until equilibrium solution (i.e., osmotic equilibrium) was reached [Figs. 13(b), 13(d), and 13(f)]. Between the central and the left pores, component 2 could pass freely through the center of the connecting channel, because the size-exclusion potential there vanishes and remains sufficiently big only near the walls of the channel. As a result, in equilibrium solution, both said pores on either side of the channel become filled with mixture of equal composition [Figs. 13(b) and 13(d)]. Equilibrium pressure in these two pores is also identical [Fig. 13(f)]. However, as expected, there is difference in both composition and pressure between the central pore and the right pore that are connected with the thinner channel and where the size-exclusion potential is big everywhere across. Here, component 2 could not pass the constriction of the channel. As a result, the forward osmotic process took place, in which a portion of component 1 passed through from the right pore despite the fact that such flow has reduced pressure in the right pore; i.e., the flow has occurred along pressure gradient.

Let us now turn to modeling of the reverse osmosis. The problem statement was as follows. The entire model was filled uniformly with component 1 at reference density [Fig. 14(a)]. Component 2 was added to the central spherical pore so that it amounted to 9.3% molar concentration [Fig. 14(c)]. As a result, in the initial time moment, pressure in the central pore was elevated above reference pressure [Fig. 14(e)]. Numerical simulation was carried out until equilibrium solution was reached.

Results of the numerical simulation by DFH are presented in Figs. 14(b), 14(d), and 14(f). Because component 2 could pass freely through the center of the wider constriction on the left, in equilibrium solution, both the left and the central pores become filled with mixture at equal composition [Figs. 14(b) and 14(d)], similar to the case of the forward osmosis simulation. Equilibrium pressure is also equal in the both pores. But again, as was in the forward osmosis scenario, the equilibrium solution is absolutely different in the pore on the right. Component 2 could not pass the constriction. Consequently, reverse osmosis process took place, in which

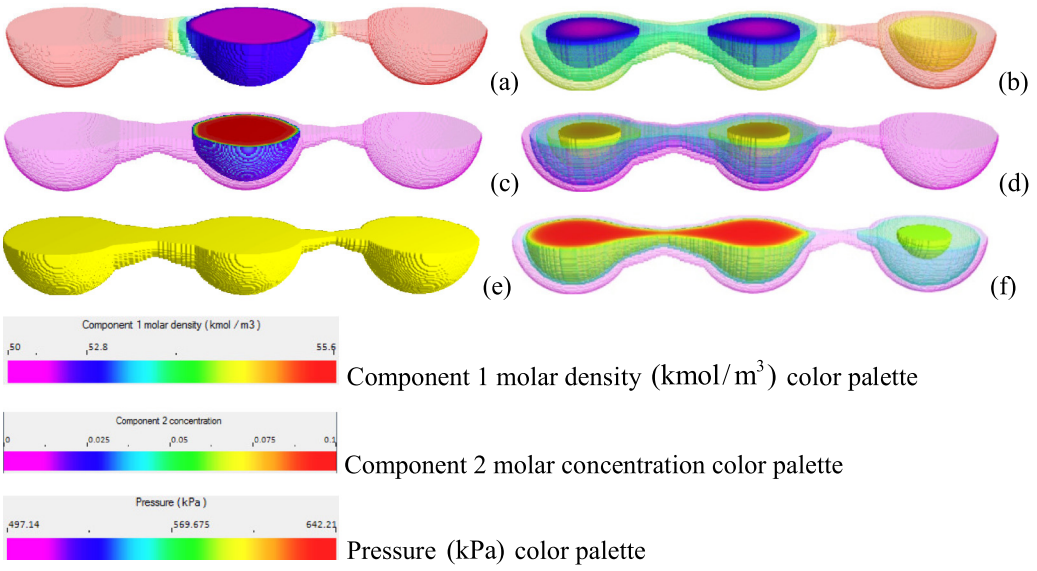

FIG. 13. 3D view in cross-section of the initial conditions (a, c, e) and the equilibrium solution (b, d, f) in the forward osmosis numerical simulation. Panels (a) and (b) show distribution of component 1 molar density, (c) and (d) show distribution of component 2 concentration, and (e) and (f) show distribution of pressure. Some of the numerical ranges are made semitransparent. The values of the parameters are shown in colors according to the color palettes.

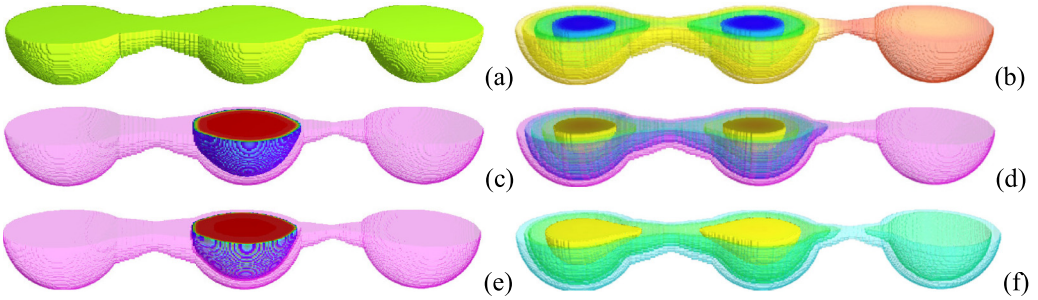

FIG. 14. 3D view in cross-section of the initial conditions (a, c, e) and the equilibrium solution (b, d, f) in the reverse osmosis numerical simulation. (a) and (b) show distribution of component 1 molar density, (c) and (d) show distribution of component 2 concentration, and (e) and (f) show distribution of pressure. Some of the numerical ranges are made semitransparent. The values of the parameters are shown in colors according to the color palettes of Fig. 13.

component 1 passed from the rest of the model to the right chamber until pressure difference at either side of the constriction reduced down to osmotic pressure.

IV. CONCLUSION

In this paper, we presented the description of liquid nanoflow phenomena in the frame of DFH. The new element introduced in the DFH modeling technique is the external potential depending on spatial coordinates. For a continuum mechanics-based method such as DFH, the external potential is a convenient way to deliver consistent description of the key nanoscale phenomena related to disjoining pressure and size-exclusion effects.

Various liquid nanoflow phenomena were captured and highlighted in the numerical results presented in this paper. We began with modeling of various types of disjoining pressure isotherms corresponding to complete wetting, partial wetting, and nonwetting. The nanoscale feature that was reproduced in numerical simulations is the presence of the nanometer scale thin film in cases exhibiting nonwetting or only partial wetting with respect to the bulk phase. Disjoining pressure profiles obtained from the numerical simulation results are in conformance with the published data.

Then we presented the modeling of spreading dynamic phenomena. The demonstrated effects include film precursor and anomalous non-Newtonian rheology of the traveling film.

Next, we presented a numerical simulation of the two-phase three-component (i.e., compositional) system in contact with the surface exhibiting heterogeneous properties. In addition to already successful incorporation of bulk and film phase coexistence, the numerical simulation results of this case demonstrate selective adsorption of components in accordance with wetting preferences of the surface.

Further on, we presented the capillary condensation for both two-phase and three-phase systems.

Finally, we demonstrated the numerical simulation of osmotic effects related to size-exclusion mechanism. Both forward and reverse osmosis were reproduced.

Our results demonstrate the way that the key liquid nanoflow phenomena and mechanisms can be captured in the frame of the continuum mechanics combined with the density functional theory.

ACKNOWLEDGMENTS

We thank Schlumberger for permission to publish this work. We are indebted to Denis Klemin and Mikhail Stukan for making internal review of this manuscript and providing us with a list of useful and constructive suggestions that we have gratefully incorporated.

APPENDIX: HELMHOLTZ FREE-ENERGY MODEL EXPRESSIONS USED IN NUMERICAL SIMULATIONS

This appendix contains description of the model Helmholtz free energy used in numerical simulation of examples present in this paper. We followed our previous experience in numerical modeling by DFH [2,13,15,69,70].

For homogeneous liquid (phase A) in thermodynamic equilibrium in the vicinity of some fixed state, Taylor series expansion for Helmholtz free energy density can be used in the form

$$f_{\mathrm{A}}(n_i) = f_{\mathrm{A}0} + f_{\mathrm{A}i}(n_i - n_{i\mathrm{A}}) + \tfrac{1}{2} f_{\mathrm{A}ij}(n_i - n_{i\mathrm{A}})(n_j - n_{j\mathrm{A}}), \tag{A1}$$

where $n_{i\mathrm{A}}, i = 1, \ldots, M$ are molar densities of the fixed state (phase A). Expansion coefficients $f_{\mathrm{A}0}$ and $f_{\mathrm{A}i}$ vanish from hydrodynamic equations when Helmholtz energy in the form of Eq. (A1) is used; therefore, only symmetric matrix $f_{\mathrm{A}ij}$ is relevant for modeling. This matrix is positive-definite for locally thermodynamically stable states. Coefficients $f_{\mathrm{A}ij}$ are related to the bulk modulus of phase A, K_{A}, by the expression $K_{\mathrm{A}} = f_{\mathrm{A}ij} n_{i\mathrm{A}} n_{j\mathrm{A}}$. In the case when there is more than one phase, the Helmholtz energy model for other bulk phases is similar to Eq. (A1). The number of parameters in matrix $f_{\mathrm{A}ij}$ depends on the number of chemical components. Some of the parameters can be used to fit experimental data or an equation of state [52]. The residual free parameters, if there are any, can be factored out by assuming additional symmetries of the matrix, for example, in a way that is most beneficial for efficiency of practical calculations. In two- and three-phase compositional mixtures, to obtain Helmholtz energy function $f(n_i)$ for an arbitrary set of molar density values n_i (not necessarily close to any bulk phase), we use numerical interpolation procedures.

For surface Helmoltz free-energy density, we use the numerical model expression

$$f_* = \xi_i n_i + \xi_0. \tag{A2}$$

Parameters ξ_0, ξ_i are chosen to be consistent with the system of two (in two-phase case) linear algebraic equations,

$$f_{*\mathrm{A}} = \xi_i n_{i\mathrm{A}} + \xi_0,\ f_{*\mathrm{B}} = \xi_i n_{i\mathrm{B}} + \xi_0, \tag{A3}$$

where $f_{*\mathrm{A}}, f_{*\mathrm{B}}$ are known values of surface energy density for phases A and B. The surface energy densities are related with the contact angle θ by the Young equation $\cos\theta = \frac{f_{*\mathrm{B}} - f_{*\mathrm{A}}}{\gamma_{\mathrm{AB}}}$. The residual degrees of freedom in the system Eq. (A3) can be factored out by fitting experimental data or surface equations of state. In the three-phase case, there are three equations in the system Eq. (A3) as well as there are three contact angles. In the two-phase, three-component case of Sec. III C, there is one equation with phase A and two equations with phase B, because phase B is considered compositional and formed of two components. The latter two equations enable one to introduce dependence of surface energy on composition of phase B.

[1] A. Demianov, O. Dinariev and N. Evseev, Can. J. Chem. Eng. **89**, 206 (2011).
[2] A. Yu. Demianov, O. Yu. Dinariev, and N. V. Evseev, *Introduction to the Density Functional Method in Hydrodynamics* (Fizmatlit, Moscow, 2014).
[3] D. M. Anderson, G. B. McFadden, and A. A. Wheeler, Annu. Rev. Fluid Mech. **30**, 139 (1998).
[4] H. A. Jakobsen, *Chemical Reactor Modelling* (Springer-Verlag, Berlin, 2008).
[5] P. Meakin and A. M. Tartakovsky, Rev. Geophys. **47**, RG3002 (2009).
[6] V. Joekar-Niasar, M. I. J. van Dijke, and S. M. Hassanizadeh, Transp. Porous Med. **94**, 461 (2012).
[7] J. Kim, Commun. Comput. Phys. **12**, 613 (2012).
[8] M. J. Blunt, B. Bijeljic, H. Dong, O. Gharbi, S. Iglauer, P. Mostaghimi, A. Paluszny, and C. Pentland, Adv. Water Resour. **51**, 197 (2013).
[9] O. Dinariev, J. Appl. Math. Mech. **59**, 745 (1995).
[10] O. Dinariev, J. Appl. Math. Mech. **62**, 397 (1998).
[11] D. Koroteev, O. Dinariev, N. Evseev, D. Klemin, A. Nadeev, S. Safonov, O. Gurpinar, S. Berg, C. van Kruijsdijk, R. Armstrong, M. T. Myers, L. Hathon, and H. de Jong, Petrophysics **55**, 294 (2014).
[12] R. T. Armstrong, N. Evseev, D. Koroteev, and S. Berg, Adv. Water Resour. **77**, 57 (2015).
[13] R. T. Armstrong, S. Berg, O. Dinariev, N. Evseev, D. Klemin, D. Koroteev, and S. Safonov, Transp. Porous Med. **112**, 577 (2016).
[14] N. Evseev, O. Dinariev, M. Hürlimann, and S. Safonov, Petrophysics **56**, 32 (2015).
[15] O. Dinariev and N. Evseev, Computat. Geosci. **20**, 835 (2016).
[16] R. G. Parr and W. Yang, *Density-Functional Theory of Atoms and Molecules* (Oxford University Press, New York, 1989).
[17] P. Hohenberg and W. Kohn, Phys. Rev. **136**, B864 (1964).
[18] W. Kohn, Rev. Mod. Phys. **71**, 1253 (1999).
[19] F. F. Abraham, Phys. Rep. **53**, 93 (1979).
[20] J.-L. Barrat and J.-P. Hansen, *Basic Concepts for Simple and Complex Liquids* (Cambridge University Press, Cambridge, 2003).
[21] T. L. Beck, M. E. Paulaitis, and L. R. Pratt, *The Potential Distribution Theorem and Models of Molecular Solutions* (Cambridge University Press, Cambridge, 2006).
[22] J. Z. Wu, in *Molecular Thermodynamics of Complex Systems*, edited by X. Lu and Y. Hu (Springer-Verlag, Berlin, 2009), pp. 1–74.
[23] R. D. Groot and J. P. van der Eerden, Phys. Rev. A **36**, 4356 (1987).
[24] A. R. Denton and N. W. Ashcroft, Phys. Rev. A **44**, 1219 (1991).
[25] P. Frodl and S. Dietrich, Phys. Rev. A **45**, 7330 (1992).
[26] D. W. Marr and A. P. Gast, Phys. Rev. E **47**, 1212 (1993).
[27] A. Pereira and S. Kalliadasis, J. Fluid Mech. **692**, 53 (2012).
[28] P. Yatsishin, N. Savva, and S. Kalliadasis, J. Chem. Phys. **142**, 034708 (2015).
[29] A. V. Neimark, P. I. Ravikovitch, and A. Vishnyakov, J. Phys.: Condens. Matter **15**, 347 (2003).
[30] J. Wu, AIChE J. **52**, 1169 (2006).
[31] J. Landers, G. Y. Gor, and A. V. Neimark, Colloid. Surface A **437**, 3 (2013).
[32] Z. Li, Z. Jin, and A. Firoozabadi, SPE J. **19**, 1096 (2014).
[33] B. D. Goddard, A. Nold, and S. Kalliadasis, J. Chem. Phys. **138**, 144904 (2013).
[34] P. C. Hohenberg and B. I. Halperin, Rev. Mod. Phys. **49**, 435 (1977).
[35] R. Evans, Adv. Phys. **28**, 143 (1979).
[36] P. R. Harrowell and D. W. Oxtoby, J. Chem. Phys. **86**, 2932 (1987).
[37] H. Emmerich, *The Diffuse Interface Approach in Material Science. Thermodynamic Concepts and Applications of Phase-Field Models* (Springer, Berlin, 2003).
[38] A. Onuki, *Phase Transition Dynamics* (Cambridge University Press, Cambridge, 2004)
[39] J. Liu, G. Amberg, and M. Do-Quang, Phys. Rev. E **93**, 013121 (2016).
[40] E. Ivanov, N. Evseev, and O. Dinariev, Proceedings of the International Conference on Heat Transfer and Fluid Flow, Prague, Czech Republic, August 11–12 (2014).
[41] B. V. Derjaguin and E. Obuchov, Acta Physicochim. URSS **5**, 1 (1936).
[42] V. M. Starov, M. G. Velarde, and C. J. Radke, *Wetting and Spreading Dynamics* (CRC Press, London, 2007).
[43] D. N. Zubarev, *Nonequilibrium Statistical Thermodynamics* (Plenum Press, New York, 1974).
[44] I. Prigogine, *Introduction to Thermodynamics of Irreversible Processes* (John-Wiley, New York, 1967).
[45] L. I. Sedov, *Mechanics of Continuous Media* (World Scientific, Singapore, 1997), Vol. 1.
[46] S. R. de Groot and P. Mazur, *Non-equilibrium Thermodynamics* (North-Holland, Amsterdam, 1962).
[47] S. Ono and S. Kondo, *Molecular Theory of Surface Tension* (Springer-Verlag, Berlin, 1960).

[48] B. V. Derjaguin, N. V. Churaev, and V. M. Muller, *Surface Forces* (Consultants Bureau, New York, 1987).
[49] H. E. Stanley, *Introduction to Phase Transitions and Critical Phenomena* (Oxford University Press, Oxford and New York, 1971)
[50] H. K. Versteeg and W. Malalasekera, *An Introduction to Computational Fluid Dynamics. The Finite Volume Method* (Longman Scientific & Technical, New York, 1995).
[51] J. H. Ferziger and M. Peric, *Computational Methods for Fluid Dynamics* (Springer-Verlag, Berlin, 2002).
[52] S. M. Walas, *Phase Equilibria in Chemical Engineering* (Butterworth-Heinemann, New York, 1985).
[53] D. Bonn, J. Eggers, J. Indekeu, J. Meunier, and E. Rolley, Rev. Mod. Phys. **81**, 739 (2009).
[54] R. V. Craster and O. K. Matar, Rev. Mod. Phys. **81**, 1131 (2009).
[55] M. N. Popescu, G. Oshanin, S. Dietrich, and A.-M. Cazabat, J. Phys.: Condens. Matter. **24**, 243102 (2012).
[56] J. R. Henderson, Phys. Rev. E **72**, 051602 (2005).
[57] J. Israelachvilli, *Intermolecular and Surface Forces* (Academic Press, San Diego, CA, 1992).
[58] B. Dai, L. G. Leal, and A. Redondo, Phys. Rev. E. **78**, 061602 (2008).
[59] L. M. Pismen and Y. Pomeau, Phys. Rev. E **62**, 2480 (2000).
[60] B. Bhushan (ed.), *Springer Handbook on Nanotechnology* (Springer-Verlag, Berlin, 2004).
[61] A. Firoozabadi, *Thermodynamics of Hydrocarbon Reservoirs* (McGraw-Hill, New York, 1999).
[62] J. Cazes and R. P. W. Scott, *Chromatography Theory* (Marcel Dekker, Inc., New York, 2002).
[63] V. M. Gun'ko, Theor. Exp. Chem. **43**, 139 (2007).
[64] S. J. Gregg and K. S. W. Sing, *Adsorption, Surface Area, and Porosity* (Academic Press, New York, 1982).
[65] A. W. Adamson and A. P. Gast, *Physical Chemistry of Surfaces* (John Wiley & Sons, New York, 1997).
[66] P. C. Hiemenz and R. Rajagopalan, *Principles of Colloid and Surface Chemistry* (Marcel Dekker, Inc., New York/Basel/Hong-Kong, 1997).
[67] N. H. Fletcher, J. Chem. Phys. **29**, 572 (1958).
[68] R. W. Baker, *Membrane Technology and Applications*, 2nd ed. (John Wiley & Sons, Chichester, West Sussex, England, 2004).
[69] A. Yu. Demyanov and O. Yu. Dinariev, Fluid Dyn. **39**, 933 (2004).
[70] A. Yu. Dem'yanov and O. Yu. Dinariev, J. Appl. Mech. Tech. Phys. **45**, 670 (2004).